scientific reports

Check for updates

OPEN

Anticancer efficacy of magnetite nanoparticles synthesized using aqueous extract of brown seaweed *Rosenvingea intricata*, South Andaman, India

V. Swathi Pon Sakthi Sri[1]✉, Y. Aron Santhosh Kumar[1], M. Savurirajan[1], Dilip Kumar Jha[1], N. V. Vinithkumar[2] & G. Dharani[2]

Cancer is a global issue and hence various efforts are being made. Iron oxide is considered a significant biochemical agent in the biomedical arena for cancer treatment. Marine macroalgae-mediated iron oxides especially, magnetite (Fe_3O_4) nanoparticles (NPs) are a prospective alternative to diagnose and treat cancer owing to their fluorescent and magnetic properties. We intend to appraise the usability of the aqueous extract of *Rosenvingea intricata* (*R. intricata*) in Fe_3O_4 NPs synthesis and to study their cytotoxic effects against human hepatocarcinoma (Hep3B) and pancreatic (PANC1) cancer cells. In the present study, *R. intricata* were collected from the coastal region of South Andaman, India. Aqueous extracts of *R. intricata* were utilized to synthesize Fe_3O_4 NPs via the co-precipitation method. Phycosynthesized Fe_3O_4 NPs exhibited wide peak at 400–600 nm from ultraviolet–visible diffused reflectance spectroscopic analysis which validated the formation of NPs. Band edge emission peak at 660 nm in fluorescent spectra confirmed the quantum confinement in Fe_3O_4 NPs. Fourier transform infrared spectroscopy confirmed the role of *R. intricata* as a capping and reducing agent with functional groups such as O–H, C–H, C=O, N=O, C=C, C–O, C–N, and C–S arising from amino acids, polysaccharides, aliphatic hydrocarbons, esters, amides, lignins, alkanes, aliphatic amines, and sulfates. Physicochemical properties such as crystallite size (14.36 nm), hydrodynamic size (84.6 nm), irregular morphology, elemental composition, particle size (125 nm), crystallinity, and saturation magnetization (0.90007 emu/g) were obtained from x-ray diffractometer, dynamic light scattering, scanning electron microscopy, energy dispersive x-ray spectrometer, high-resolution transmission electron microscopy, selected area electron diffraction and vibrating sample magnetometer techniques, respectively. The cell viability showed dose-dependent cytotoxic effects and enhanced the apoptosis against Hep3B and PANC1 cancer cells. *R. intricata* extract capped Fe_3O_4 NPs could be the most appropriate and effective nanomaterial for cancer treatment and management.

Keywords *Rosenvingea intricata*, Magnetite, Nanotechnology, Biomolecules, Cancer, Apoptosis

Cancer is one of the major reasons for mortality worldwide and is a great apprehension among researchers for therapeutic findings[1]. The World Health Organization (WHO) has stated that by 2040, it is expected to reach 27.5 million new cancer cases and 16.3 million mortalities[2]. It is instigated by uninhibited uncharacteristic cell development[1]. At present, chemotherapy and radiation therapy are leading in the treatment of cancer which has substantial side effects like hair loss, nausea, vomiting, reduced red blood cells, deficiency of leukocytes, and low platelet count which affects the patient's well-being and quality of life during treatment[3]. Hence, the necessity to find an efficient treatment to overcome the disadvantages of the above treatment must be found[4]. Herein, nanomedicine is a significant root that finds a solution to cure cancer and kill cancerous cells using different

[1]Atal Centre for Ocean Science and Technology for Islands (ACOSTI), National Institute of Ocean Technology (NIOT), Port Blair, India. [2]Marine Biotechnology Division, Ministry of Earth Sciences, National Institute of Ocean Technology (NIOT), Goverment of India, Pallikaranai, Chennai, India. ✉email: swathiponsakthisri@gmail.com; swathiv-proj.niot@gov.in

nanoparticles (NPs) without many side effects[5]. Nanotechnology deals with materials at the molecular level and has enormously reformed the arena of science[6]. NPs with size 1–100 nm have eminent properties compared to bulk materials[7].

Several methods are available for the synthesis of NPs including physical and chemical methods with the use of toxic chemicals that are exclusive and injurious to human beings[8]. Hence, evolved the greener approach for the nontoxic synthesis of NPs using aqueous extracts of different organisms like plants[9,10], algae[11,12], bacteria[13,14], and fungi[15–17]. Amongst these, algae-assisted production of NPs is comparatively less discovered. This method is not only cost-effective but causes insignificant menace to ecological health[18]. Although, algae are abundantly present in bulk extents at coastal areas[19,20]. However, less research has been carried out globally.

Seaweed or macroalgae is a significant renewable source in the coastal area. Red, brown, and green seaweeds play crucial roles in developing several pharmaceutical products[21]. In the field of medicine, seaweeds are widely used to cure stones in gall bladder, stomach disorders, eczema, cancer, kidney failure, scabies, asthma, atherosclerosis, cardiovascular disorders, lung ailments, ulcers, etc.[22]. The presence of biomolecules such as terpenoids, sterols, lectins, pigments, phlorotannins, ketones, alkanes, fatty acids, polysaccharides, carotenoid, glycoproteins, haloforms, hydroquinones, and phenolic compounds aids the use of seaweeds for drug discovery[23]. In the past decades, derivatives of brown seaweed *Rosenvingea intricata* (*R. intricata*) have shown antifungal, anticancer, antiallergic, antidiabetic, antiaging, anti-inflammatory, and antioxidant activities[24]. Seaweed-mediated NPs have been demonstrated as efficient nanomaterials for the treatment of cancer[25].

Metal oxide NPs are assumed to be stable and benign for human beings and among iron oxide NPs especially magnetite (Fe_3O_4) being a semiconductor material finds applications in wastewater decontamination, sensors, purging of organic dyes, carbon capture, energy devices, magnetic storage devices, magnetic hyperthermia treatment, targeted drug delivery, and crop development[26,27]. Realizing the medical importance of *R. intricata* and Fe_3O_4 NPs, the objectives of this work are as follows: (1) Synthesis of Fe_3O_4 NPs using aqueous extract of *R. intricata*, (2) characterization of Fe_3O_4 NPs using various spectroscopic techniques and (3) testing its efficacy against human hepatocarcinoma (Hep3B) and pancreatic (PANC1) cancer cells. Hence, Fe_3O_4 NPs were synthesized using an aqueous extract of *R. intricata* collected from the tropical coastal region of Collinpur, South Andaman, India. Synthesized Fe_3O_4 NPs were characterized using various spectroscopic methods. 3-(4,5-dimethylethiazol-2-yl)-2,5-diphenyltetrazolium bromide (MTT) assay, morphological analysis and dual staining assay were used to determine the anticancer efficacy of *R. intricata* mediated Fe_3O_4 NPs.

Materials and methods

Study area description

Mature and well-grown thallus of *R. intricata* were collected from the coastal area of the Collinpur region, which was sandy coast along with various types of rocky substratum spread over the shoreline that helps in the sustenance of the luxuriant development of seaweed flora. Latitude (11° 41′ 33.9" N) and Longitude (92° 35′ 55.1"E) of *R. intricata* collection site was noted from handheld GPS (Garmin etrex Vista H), and the study area map (Fig. 1) was generated using ArcGIS software (ArcGIS, Version: 10.8.2).

Collection and identification of seaweed

The collected seaweed sample was preserved and species-level identification was done based on the external and internal morphology of specimens and sourcing the original protocol and standard flora[28]. *Rosenvingea intricata* (=*Rosenvingea endiviifolia*) is one of the lesser-known wild species that dwell in the east (Tamil Nadu and Andhra Pradesh) and west coast (Gujarat) of India and Andaman Nicobar Islands[21,29,30]. For the present study, the biomass of this species was collected from the Collinpur region of South Andaman. The species level of identification is done by acquiring the morphological and anatomical character sourcing the original protologue of the species[31] and referring to the standard Indian seaweed flora[29,32,33]. The collected specimens have been preserved in the form of herbarium (Specimen No: ACOSTI-NIOT-027) and deposited at the Atal Centre for Ocean Science and Technology, National Institute of Ocean Technology, Port Blair.

Processing of seaweed

The collected seaweed sample was well rinsed with seawater followed by freshwater and Milli Q water to eliminate all debris such as epiphytes, sand particles including other adhering detritus materials. The water content in the seaweed sample was removed using blotting sheets. Cleaned seaweed was shade-dried for 5–7 days and destined for pulverization to get a coarse powder[34,35].

Preparation of aqueous extract of *R. intricata*

10 g dry powder of *R. intricata* was mixed with 100 mL milli Q water and boiled at 90 °C for 15 min. It was vacuum-filtered to yield the aqueous extract of *R. intricata*. Stored at -4 °C for further usage.

Phycosynthesis of Fe_3O_4 NPs using aqueous extract of *R. intricata*

To 50 mL aqueous extract of *R. intricata*, 0.6 molar (M) ferric chloride hexahydrate ($FeCl_3.6H_2O$) was added and stirred for 1 h at 80 °C at 600 rpm. Further, 0.5 M sodium hydroxide (NaOH) was added dropwise to this for the precipitation of NPs. pH is maintained to be 11 (Fig. 2). It was further stirred for 30 min, centrifuged, and dried in a hot air oven (Model: ASI-HO-121212) at 60 °C. Powdered using an agate mortar and pestle[11].

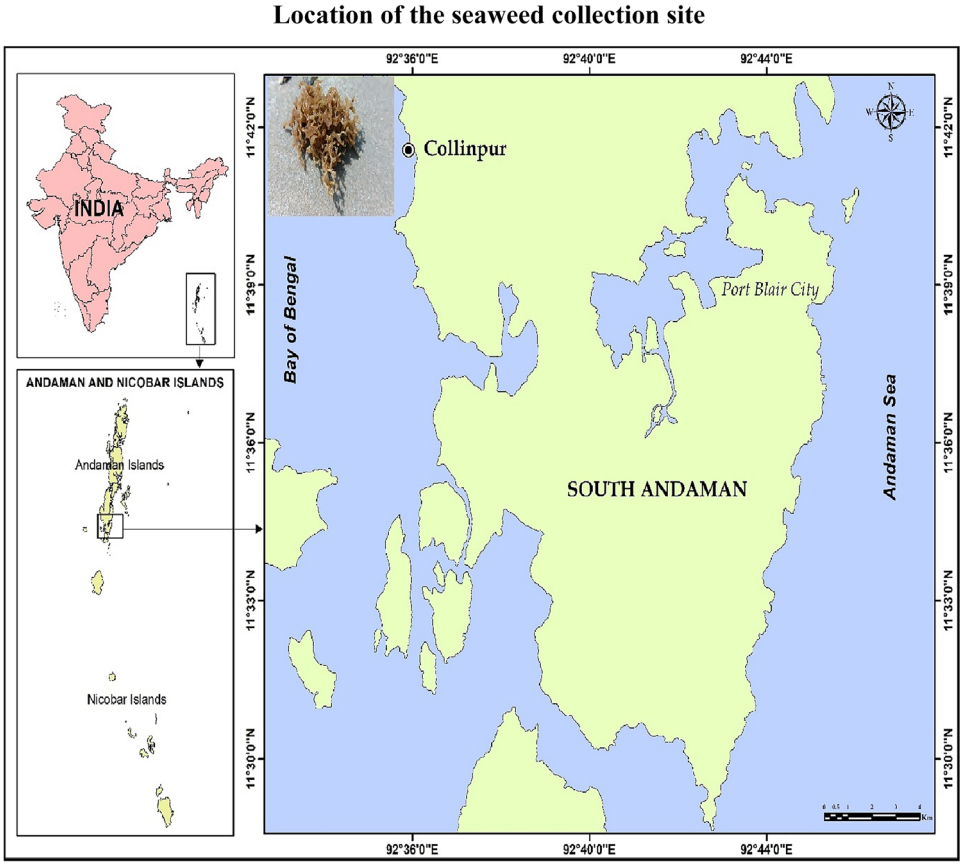

Figure 1. Location of the seaweed collection site map (ArcGIS 10.8.2, inset: *R. intricata*).

Characterization of Fe_3O_4 NPs

Various methods for the description of synthesized Fe_3O_4 NPs in the present work were used for NPs characterization such as:

Ultra violet-visible diffused reflectance spectrophotometer (UV–Vis DRS)

The optical behavior of Fe_3O_4 NPs obtained using an aqueous extract of *R. intricata* was analyzed using UV–Vis DRS (Model: Jasco V-750). The sample was prepared by compacting it into a wafer and fitting the wafer to the reflectance sample holder. Optical band gap energy is estimated using Eq. (1).

$$\alpha h\upsilon = (h\upsilon - E_g)^n \tag{1}$$

where α = absorption coefficient, hν = photon energy, E_g = optical band gap energy, and n = ½ for a direct transition[36].

Fluorescence analysis

Fluorescence property was studied using a fluorometer (Model: PerkinElmer LS 45)[32]. *R. intricata*-mediated Fe_3O_4 NPs were diluted with Milli Q water and the fluorescence spectra were attained by exciting the sample using LED lamps with a resolution of 0.5 nm.

Fourier transform infra-red spectrometer (FTIR)

Biomolecules adhered to the sample were premeditated using FTIR (Model: PerkinElmer Spectrum Two)[36]. Briefly, 3 mg *R. intricata*-mediated Fe_3O_4 NPs was mixed and ground in an agate mortar with 250 mg of pure spectroscopic grade potassium bromide (KBr) earlier dried at 300 °C in a muffle furnace (Model: Gefran 400) for 4 days. The ultrapure transparent pellet of 13 mm diameter was attained by smearing a force weight of 10 tons for nearly 10 min. IR absorbance was scanned in the range 450–4000 cm^{-1}.

X-Ray diffractometer (XRD)

Crystalline phases of Fe_3O_4 NPs were analyzed using XRD (Model: Bruker D8 Advance) with a Cu radiation source. Briefly, the sample was ground into a fine powder using an agate mortar and pestle. It was filled in the empty sample holder and gently pressed using a glass slide. The excess sample was removed from the sample

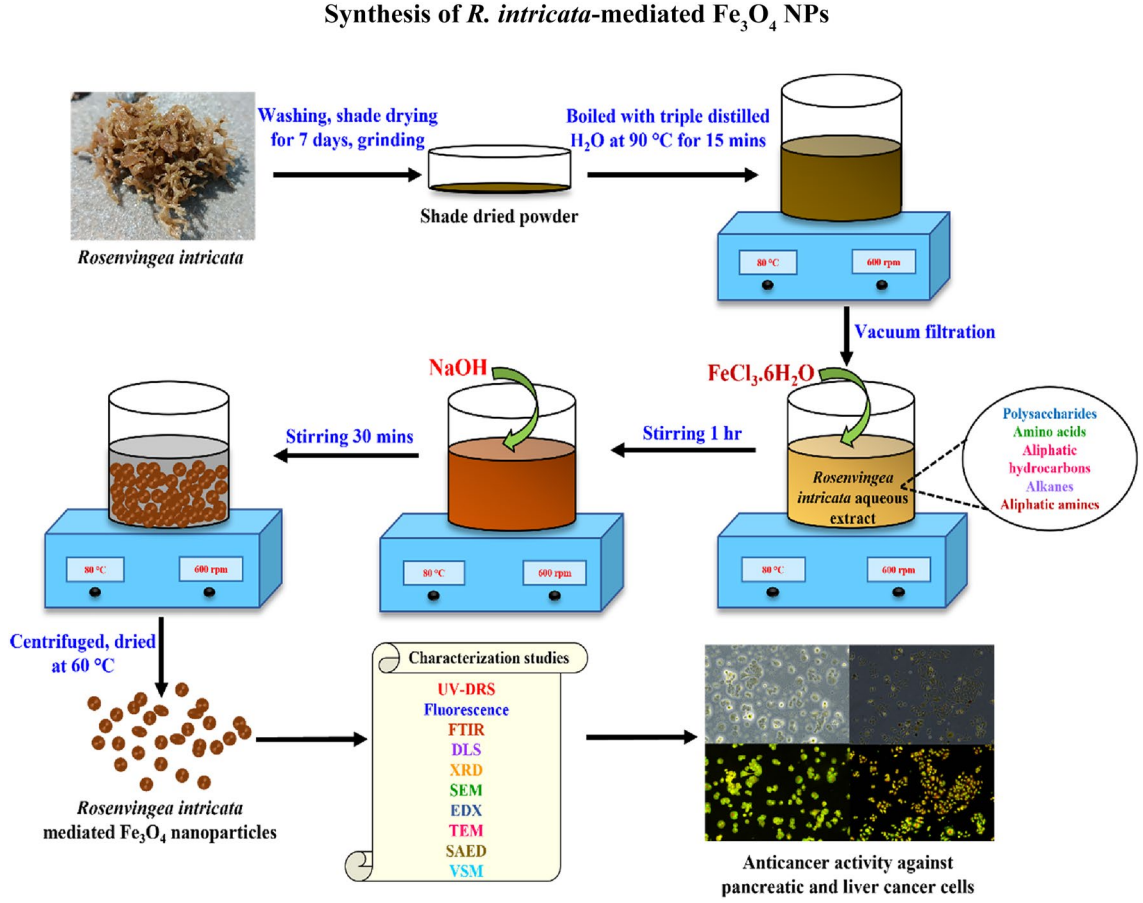

Figure 2. Schematic illustration of *R. intricata*-mediated phycosynthesis of Fe_3O_4 NPs as a promising agent against pancreatic and liver cancer cells.

holder edges. The sample holder was carefully placed in the XRD slot. Scanned in the range of 20°–70°. The crystallite size was determined using Scherrer's Eq. (2):

$$D = K\lambda/\beta Cos\theta \quad (2)$$

where D = crystallite size (nm), K = shape factor, λ = wavelength of X-ray radiation, β = full with at half maximum (FWHM) and θ = Bragg angle[36].

Dynamic light scattering (DLS)

Measurement of size is a main stage in the design of NPs production and its thriving usage. DLS utilizes scattered light to measure the extent of diffusion in nanomaterials[29,30]. Particle size measurement was done using DLS (Model: Micromeritics Nano Plus). Fe_3O_4 NPs are distributed in Milli Q water and sonicated for 30 min. The measurement state is maintained with a refractive index of 1.3328 and viscosity of the dispersion as 0.8878 (cP) at temperature 25° C[36,37].

High-resolution scanning electron microscope (HRSEM) coupled with energy dispersive X-ray spectrometer (EDX)

HRSEM analysis is apt for the visualization of the morphology and size of the nanomaterials with their exterior texture[35]. The sample was mounted on a stub of metal with adhesive coated with gold and then visualized in the scanning electron microscope HRSEM (Model: F E I Quanta FEG 200). HRSEM coupled with EDX was used for the elemental profiling[36].

High-resolution transmission electron microscope (HRTEM) coupled with selected area electron diffraction (SAED)

Surface texture and particle size were observed using HRTEM (Model: Jeol/JEM 2100). The sample was prepared through drop-coating on carbon-coated TEM grids[36]. HRTEM coupled with SAED was used for the identification of crystalline phases of Fe_3O_4 NPs[36]. The d spacing was calculated using the electron diffraction Eq. (3)

$$L\lambda = dR \quad (3)$$

where L is the distance between the sample and electron micrograph, λ is the X-ray wavelength, and R is the radius of diffraction rings[26,36].

Vibrating sample magnetometer (VSM)
Magnetic properties of *R. intricata*-mediated Fe_3O_4 NPs are determined using VSM (Model: Lakeshore, USA, 7407) at moderate conditions and the magnetization value is analytically noted with the applied magnetic field to an extent of 15,000 Gauss. The squareness ratio is estimated using relation (4).

$$\text{Squareness ratio} = \frac{M_r}{M_s} \tag{4}$$

where M_r = remanent magnetization and M_s = saturation magnetization[36,37].

Anticancer studies

Cell culture conditions
The Human liver cancer cells Hep3B and pancreatic cancer cells PANC1 were purchased from the National Centre for Cell Science (NCCS, Pune, India). Cells were cultured in Dulbecco's modified Eagle's medium with high glucose (DMEM-HG) media ((Make: Himedia; Cat No: AT151-5L)) containing 10% FBS (Make: Himedia; at No: RM9955-500 ml), Antibiotic Antimycotic solution 100X (Make: Himedia; Cat No: A002) and 37 °C temperature provided with 5% CO_2. During subculture, once every 2–3 days, the medium was replaced with a fresh one. Cell-based experiments were performed after reaching 80% to 90% confluency.

In vitro cytotoxic studies using MTT assay
The human liver cancer cells (Hep3B) and human pancreatic cancer cells (PANC1) cells (Table 1) were independently seeded (1 X 10^4 cells/well) in 96 well plates with DMEM medium augmented with 10% FBS, 1X Antibiotic Antimycotic solution in CO_2 incubator at 37 °C with 5% CO_2. Cells were washed with 200 µL of 1 × phosphate-buffered saline (PBS), afterwards the cells were treated with different doses of *R. intricata*-mediated Fe_3O_4 NPs (25, 50, 100, 250, and 500 µg/mL) and with half-maximal inhibitory concentration (IC_{50}) of Doxorubicin (3.87 µg/mL for Hep3B) and (8 µg/mL for PANC1)) as a positive control in serum-free DMEM medium and incubated for 24 h. The medium was aspirated from cells towards the end of the treatment period. Subsequently, the cells were washed with sterile PBS and imaged using an inverted phase contrast microscope (Make: Optika, Germany). MTT (0.5 mg/mL) prepared in 1 × PBS was added to 100 µl which was added to each well and incubated for a period of 4 h at 37 °C in a CO_2 incubator. Once the incubation time was accomplished, the MTT was cast off from the cells and washed using 200 µL of PBS. The washing phase is for the exclusion of residual non-reduced MTT in the supernatant. Formed formazan crystals were dissolved in 100 µL of dimethyl sulfoxide (DMSO) and carefully mixed. Progress of color intensity was estimated at 570 nm. The dissolution of formazan crystals yielded a purple-blue color. Absorbance was measured at 570 nm using a microplate reader (Model: Lark LIPR-9608). Blank well contained only medium served as a negative control. Experiments were repeated thrice and the IC_{50} values were attained from the mean of triplicate measurements[36–38]. The amount of cytotoxicity was evaluated from the MTT protocol. From produced purple formazan crystals, the metabolic functioning of live cells is measured[37].

The Percentage of cell viability is calculated using Eq. (5).

$$\text{Percentage of cell viability} = \frac{\text{OD Control} - \text{OD sample}}{\text{OD Control}} \times 100\% \tag{5}$$

where OD control = absorbance value of untreated cells, OD sample = absorbance value of treated cells[37].

Morphological analysis
Hep3B and PANC1 cancer cells were cultured on a coverslip in DMEM medium overnight and treated with *R. intricata*-mediated Fe_3O_4 NPs for 24 h. Then, the medium was discarded and washed with 1 × PBS, later the coverslip was fixed with ethanol and acetic acid solution (3:1 v/v). Coverslips were slightly placed on glass slides and the change in shape of cells was detected using a phase contrast microscope[38].

Apoptosis analysis using acridine orange/ethidium iodide assay
Apoptosis is a biotic progression usually categorized by dissimilar structural phenomena by actuating the precise signaling pathways counting the caspase death receptor pathway[39]. Hep3B and PANC1 cancer cells were developed individually in a 6-well plate for 24 h before attachment. Cells were treated with IC_{50} concentrations of *R. intricata*-mediated Fe_3O_4 NPs and incubated for 24 h in a CO_2 incubator. The cells were trypsinized, centrifuged, washed twice with 1 × PBS, and resuspended in PBS solution. The cell suspension was withdrawn on the slide trailed by adding 1 mL of acridine orange (1 mg/mL) and 1 mL of ethidium bromide (1 mg/mL) and placed with a coverslip. Additional fluorescent dye was washed with PBS and the apoptotic features were captured under a fluorescence microscope[38].

Cell line	Organism	Morphology	Tissue	Disease
Hep3B	Human	Epithelial	Liver	Hepatocellular carcinoma
PANC1	Human	Epithelial	Pancreas	Pancreatic carcinoma

Table 1. Details of cell lines used.

Statistical analysis

All tests were conducted a minimum of thrice in triplicate. T-test was used for the approximation of intergroup variations using GraphPad Prism 5 software. The data was expressed as mean and standard error mean (SEM). When a *p* value was fewer than 0.05, it was assumed statistically substantial.

Results and discussion

Optical properties of *Rosenvingea* intricata-mediated Fe_3O_4 NPs

UV-DRS analysis

The absorbance peak at 260 nm (Fig. 3a) corresponds to the transition of ligand to metal charge transfer (LMCT) in the tetra-coordinated Fe^{3+} (t_1—t_2 and t_1—e) and the broadness in the peak around 400–550 nm was accredited to the existence of Fe^{3+} and Fe^{2+} ions at the octahedral sites. Also, the enlargement of the absorbance band denotes NPs synthesis. Peak amplification owes to the oxygen to metal charge transfer (O^{2-} –Fe^{3+})[40]. The direct optical band gap was calculated to be 2.30 eV by inferring the tangent curve[41] (Fig. 3b).

Band gap arises due to the electrically conductive nature of a material. Semiconductors are materials with a narrow band gap. The versatility of semiconductors is that this optical phenomenon makes these materials appropriate for photocatalytic and antiaging applications. The band gap is calculated to be 2.30 eV which is quite narrow proving the possibility of using *R. intricata*-mediated Fe_3O_4 NPs in sunscreen lotions and wastewater treatment plants as catalysts[37].

Fluorescence analysis

The fluorescence spectrum (Fig. 4) of *R. intricata*-mediated Fe_3O_4 NPs exhibited sturdy emission with an intense peak at 660 nm which is credited to the band edge emission and the external imperfections arising from iron vacancy at the tetrahedral site. Surfactants capped Fe_3O_4 NPs depict sharp emission which deters NPs from energy exchange with the neighboring atoms and disrupts the expansion of the wave function of an electron. This phenomenon is owing to the effect of quantum confinement and the surface state in nanometers and biomolecule interactions. Biogenic capping agents enable control over particle size thereby enhancing intense fluorescence and in biological applications, it aids biofunctionalization for better adherence of biomolecules and drugs. During the explosion process, the emission is an indication of the production of ions. Some of these ions get stuck to the exterior part of NPs and produce emissive centers. Supposed fluorescence is caused by the interface between emissive centers and the interface surrounding. Some allowed transitions are permitted through this emission superficial interface energy bands. Symbolically, semiconductor NPs holding photoexcited charge carriers possess a crucial part in medical and environmental arenas. Especially, for localized cancer treatment and wastewater decontamination, emission-bound excitation in NPs makes them competing materials[37,42].

Structural properties of *R. intricata* mediated Fe_3O_4 NPs

FTIR analysis

Table 2 and Fig. 5 depict the FTIR spectrum data of the seaweed aqueous extract and *R. intricata*-mediated Fe_3O_4 NPs. Strong absorption around 3430 cm^{-1} and 3420 cm^{-1} is due to the existence of O–H groups from the polysaccharides and amino acids, inherent to seaweeds. These electron-rich biomolecules with hydroxyl (OH^-) groups arising from amino acids and polysaccharides have the efficacy of reducing iron ions (Fe^{3+} and

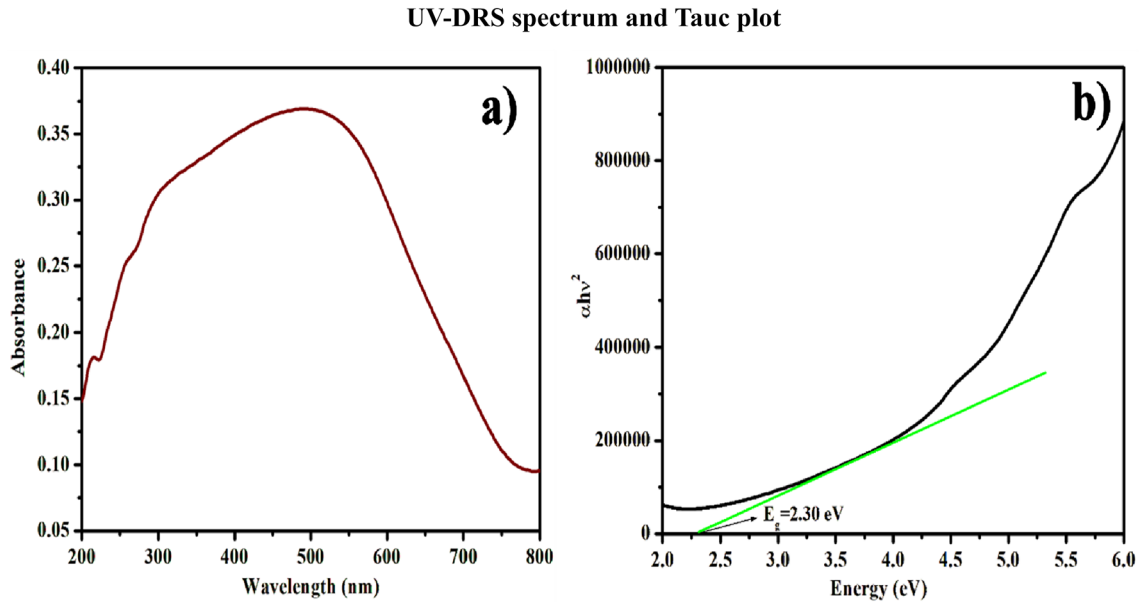

Figure 3. (**a**) Ultraviolet–visible spectrum and (**b**) Tauc plot for direct optical band gap of *R. intricata* aqueous extract-mediated Fe_3O_4 NPs.

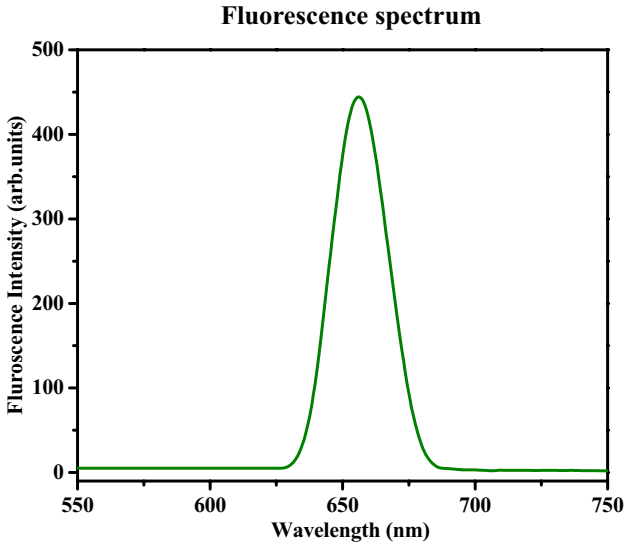

Figure 4. Fluorescence spectrum of *R. intricata* aqueous extract-mediated Fe_3O_4 NPs.

Functional groups	IR signal in *R. intricata* aqueous extract	IR signal in *R. intricata* aqueous extract mediated Fe_3O_4 NPs	References
O–H stretch of polysaccharides and amino acids	3430	3420	Sonbol et al.[5]
C–H stretch of aliphatic hydrocarbons	–	2927	Ali et al.[27]
C–H stretch	2027	2026	Sonbol et al.[5]
C=O and N=O stretch of esters and amides and C=C stretch of lignin	1634	1630	Li et al. [44]
C–N stretch and C–H bending of alkanes	–	1458	Sonbol et al.[5]
C–O stretch and O–H bending	1355	1385, 1345	Sonbol et al.[5]
C–O stretch of ring-oxygen	1271	1271	Sonbol et al.[5]
C–N stretch of aliphatic amines	1119, 1016	1119, 1020	Wang et al.[46]
C–S stretch of sulfates	620	–	Kumar et al.[47]
Fe–O stretch of ferrites	–	613, 438	SakthiSri et al.[51]

Table 2. FTIR analysis of functional group assignment.

Fe^{2+}) from their trivalent and divalent oxidation states into metallic Fe^0. Further, the chemical activity aided by these functional groups converts zero-valent iron into magnetite NPs[5]. The short peak at 2927 cm^{-1} validates the existence of a C–H stretch of aliphatic hydrocarbons[43]. Peaks at 2027 cm^{-1} and 2026 cm^{-1} are due to the C–H stretching vibrations[5]. Strong bands at 1634 cm^{-1} and 1630 cm^{-1} denoted C=O, N=O stretch signifying a mark of ester and amide causative for distinguishing essence of seaweed and also confirming the presence of lignin with (C=C) group[44]. The peak at 1458 cm^{-1} is due to the C–N stretching vibration and C–H bending mode of alkanes[5]. Peaks around 1355 cm^{-1}, 1385 cm^{-1}, and 1345 cm^{-1} signify the C–O stretching and O–H bending vibrations[5]. Peaks overhead 1271 cm^{-1} denote the phenol groups which are characteristic of seaweeds with excess antioxidants, that could be employed in the progress of efficient food and their extract could be a potential candidate in nutraceutical preparation. This peak denotes the C–O stretching of ring oxygen[5,45]. Peaks at 1119 cm^{-1}, 1016 cm^{-1}, 1119 cm^{-1} and 1020 cm^{-1} confirmed the C–N stretch of aliphatic amines[46]. Feeble absorption at 620 cm^{-1} is indicative of S=O, C–S, and C=S modes of sulfates existing in the seaweed[47]. *R. intricata* possesses polysaccharides, amino acids, aliphatic hydrocarbons, alkanes, aliphatic amines, and sulfides, which are the major biomolecules present in it. It is believed that aquatic macroalgae produce a varied diversity of organic constituents that are accountable for their distinctive essence and freshness[48]. Peaks at 613 cm^{-1} and 438 cm^{-1} of *R. intricata*-mediated Fe_3O_4 NPs denote the Fe–O stretch of ferrites[36].

XRD analysis

XRD is a suitable method to analyze the crystalline property of a material[49]. Figure 6 denoted the XRD pattern of *R. intricata* aqueous extract-mediated Fe_3O_4 NPs. Broad peaks at $2\theta = 30.42°$, 35.44°, 43.11°, 57.02°, and 63.15° resemble (220), (311), (400), (511) and (440) planes of magnetite Fe_3O_4 with an inverse cubic spinel structure (JCPDS file no. 89–2355)[36].

The crystallite size was appraised to be 14.36 nm using Scherrer's equation.

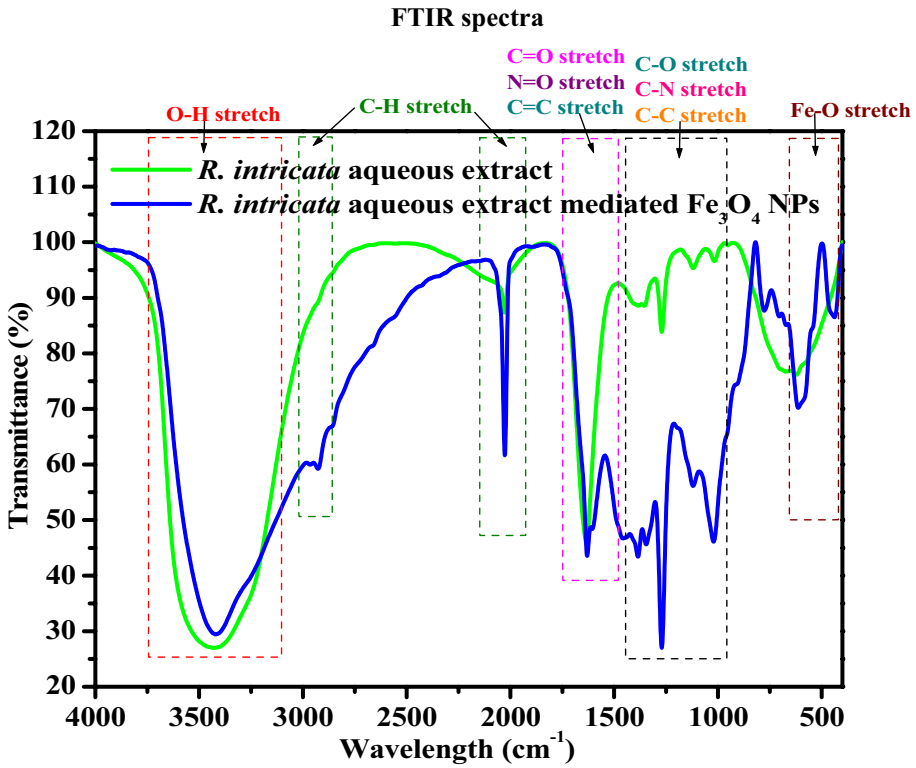

Figure 5. FTIR spectra of aqueous extract of *R. intricata* and its aqueous extract-mediated Fe_3O_4 NPs.

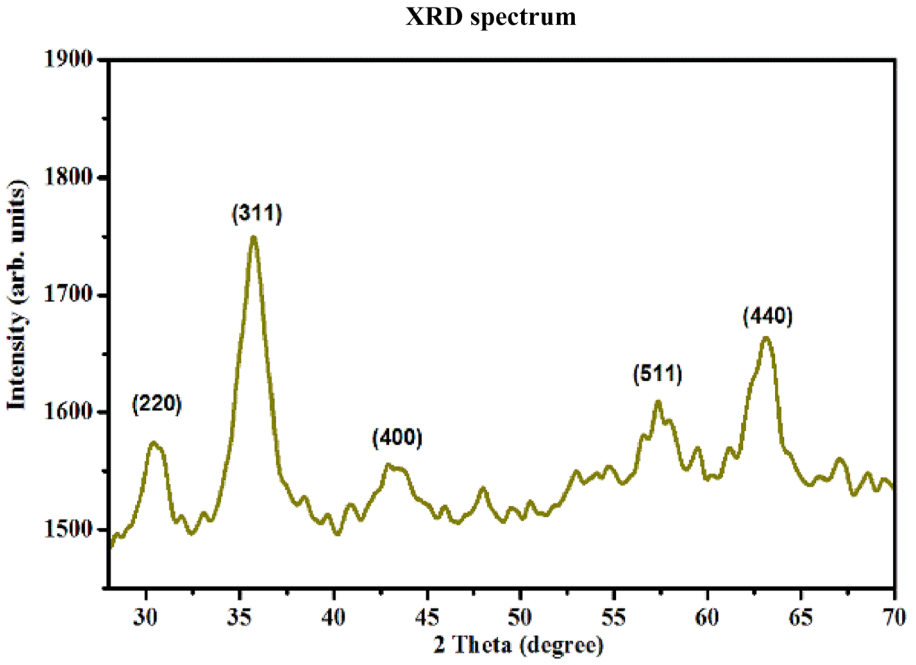

Figure 6. XRD spectra of *R. intricata* aqueous extract-mediated Fe_3O_4 NPs.

DLS analysis

Hydrodynamic particle size distribution was analyzed with a light scattering technique revealing that the average particle size of Fe_3O_4 NPs in colloidal dispersion is measured to be 84.6 ± 4.6 nm (Fig. 7) with a polydispersity index (PDI) of 0.479. It is observed that the size distribution of Fe_3O_4 NPs is much unvarying with a narrow distribution range[36].

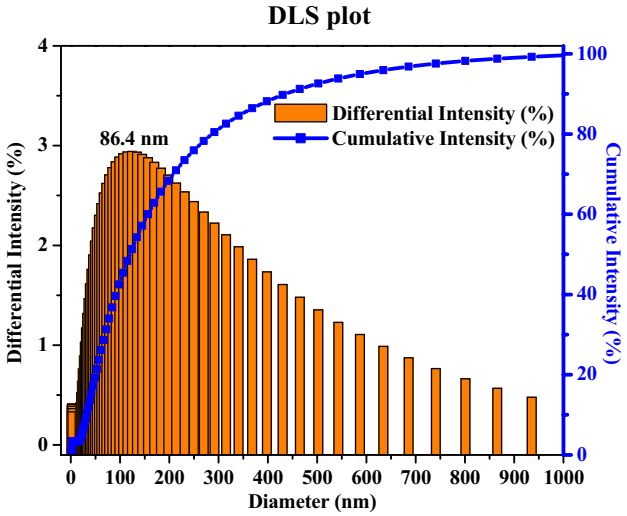

Figure 7. DLS plot of *R. intricata* aqueous extract-mediated Fe_3O_4 NPs.

Morphological properties of *R. intricata* mediated Fe_3O_4 NPs

SEM with EDX analysis

HRSEM analysis (Fig. 8a and b) confirmed the irregular shape with minor agglomerates with a rough surface. HRSEM coupled with EDX confirmed the presence of iron at 0.8, 6.3, and 6.9 keV in higher levels with minimum levels of carbon, chlorine, and sodium from the seaweed extract[50]. Peak at 0.5 keV signifies the occurrence of oxygen with a weight percent of 19.74% (Fig. 9a and b). The presence of iron and oxygen to maximum denotes the successful synthesis of Fe_3O_4 NPs.

TEM with SAED analysis

HRTEM investigation proved the uniform size distribution, shape, and defects in the structure. HRTEM images (Fig. 10a and b), confirm the spherical-shaped NPs with a size of 125 nm and lattice fringe of 0.19 nm denoting the plane (400). The mean particle size distribution is 125 nm (Fig. 10c). SAED pattern (Fig. 10d) displays well-defined concentric bright circles aligned to the planes obtained from XRD data. Concentric bright circles consisting of small dots confirmed that the *R. intricata-mediated* Fe_3O_4 is highly crystalline. The existence of distinctive rings with tiny spots denoted the presence of planes conforming magnetite[36,51].

Magnetic properties of *R. intricata*-mediated Fe_3O_4 NPs

VSM analysis

VSM hysteresis loop (Fig. 11) discloses that the synthesized material is superparamagnetic with saturation magnetization (M_s), remanent magnetization (M_r), and coercivity (B_c) values as 0.90007 emu/g, 0.17876 emu/g, and 335.72 G. Reduced magnetization (M_s) arises from spherical form, smaller size, exterior anisotropy, and disordered spins at NPs exterior layer[37]. The squareness ratio is estimated to be 0.1986. A squareness ratio less than 0.5 is a symbolic sign of small single-domain, randomly arranged spherical particles. Superparamagnetic nature aids in targeted drug delivery in cancer treatment[36,37].

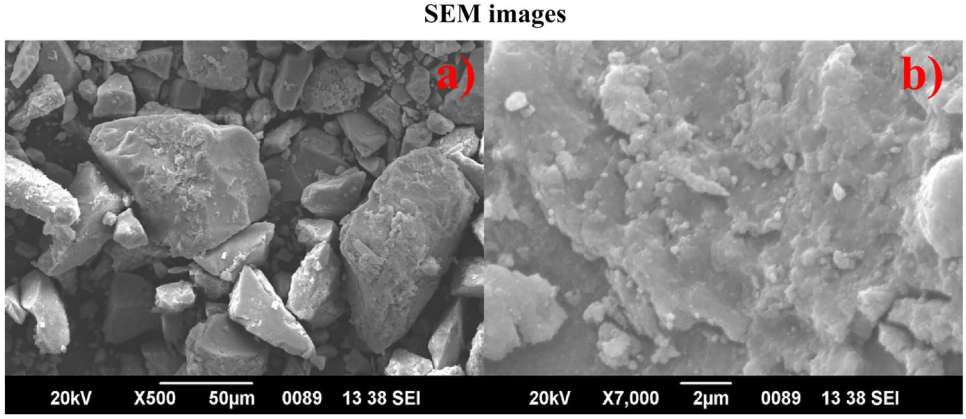

Figure 8. (**a**) and (**b**) HRSEM images of *R. intricata* aqueous extract-mediated Fe_3O_4 NPs.

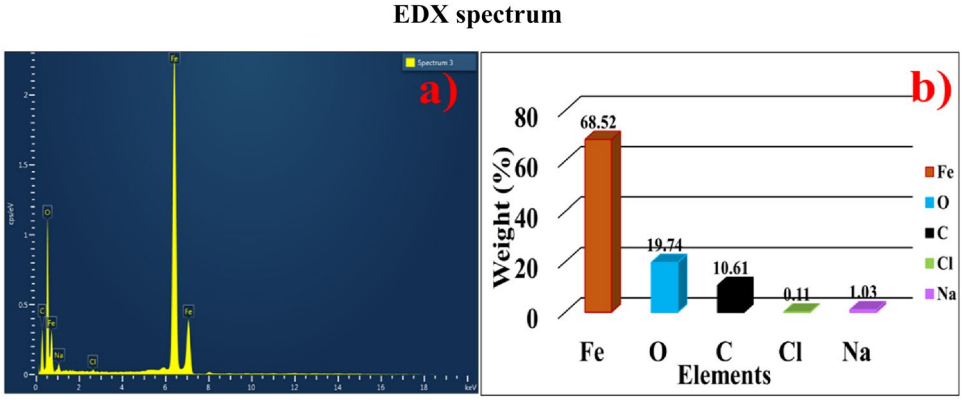

Figure 9. (**a**) EDX spectrum and (**b**) Bar graph of elemental constituents of *R. intricata* aqueous extract-mediated Fe_3O_4 NPs.

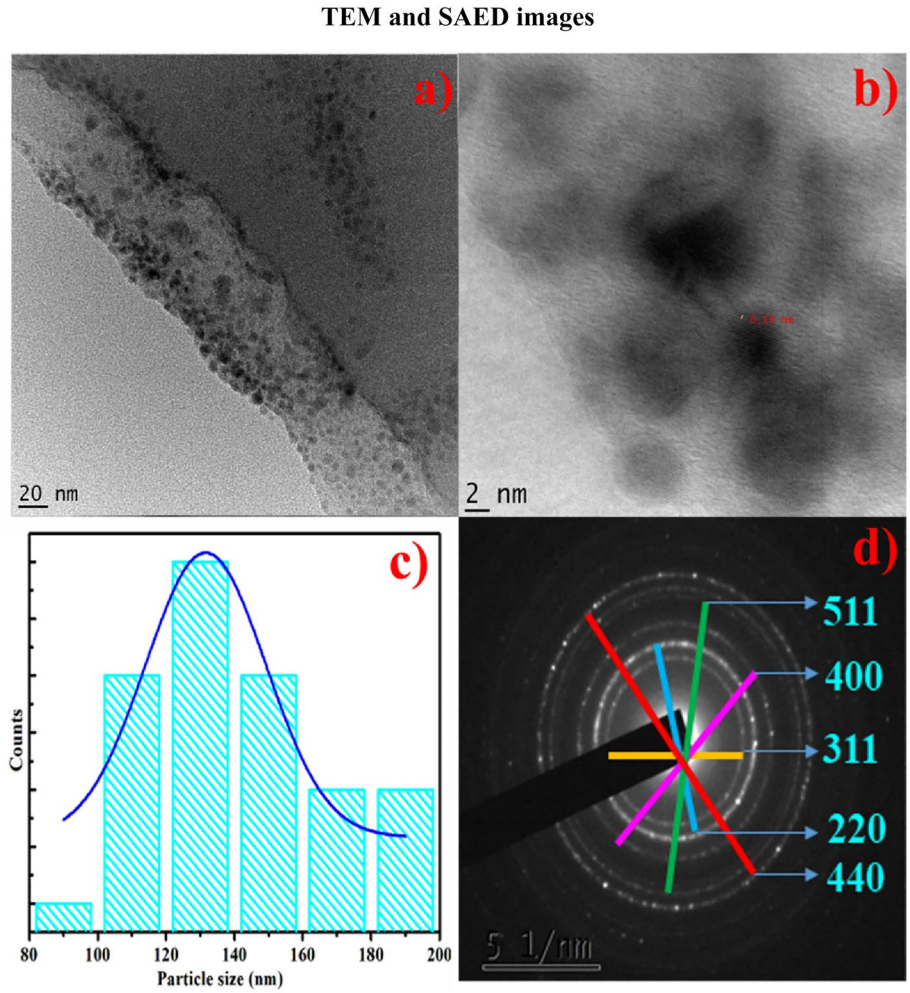

Figure 10. (**a**) TEM image and (**b**) HRTEM image (**c**) Particle size histogram and d) SAED pattern of *R. intricata* aqueous extract-mediated Fe_3O_4 NPs.

Anticancer properties of *R. intricata* mediated Fe_3O_4 NPs

MTT assay

Cytotoxicity of *R. intricata* mediated Fe_3O_4 NPs studied against Hep3B and PANC1 human liver and pancreatic cancer cells exhibited dose-dependent effect. The impact of *R. intricata*-mediated Fe_3O_4 NPs on live cells is expressed (Figs. 12 and 13; Table 3). From linear regression, IC_{50} values are calculated as 311.7 µg/mL against

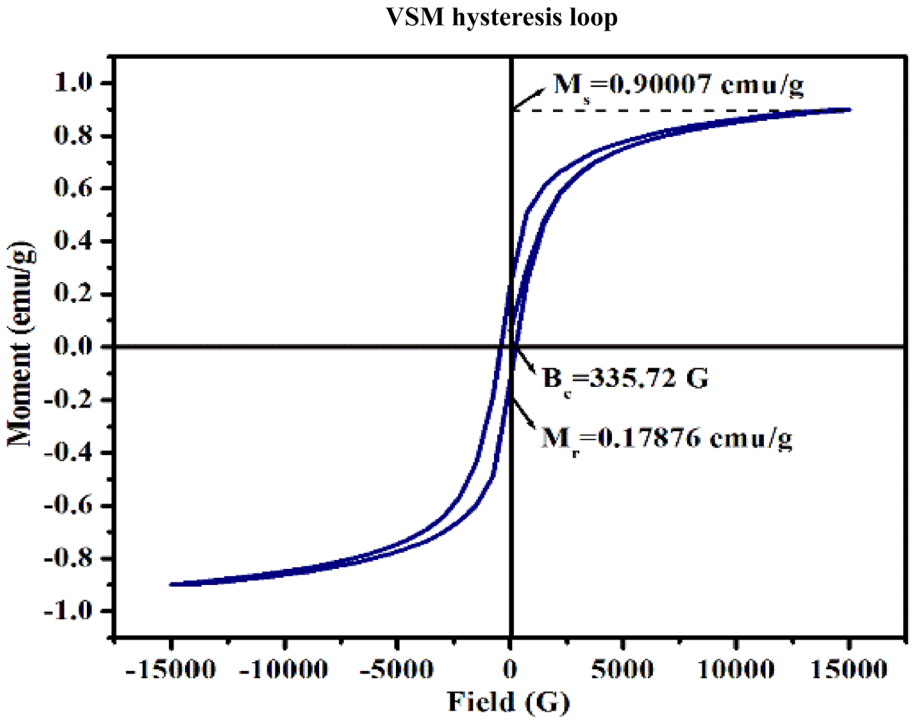

Figure 11. VSM hysteresis curve of *R. intricata* aqueous extract mediated Fe_3O_4 NPs.

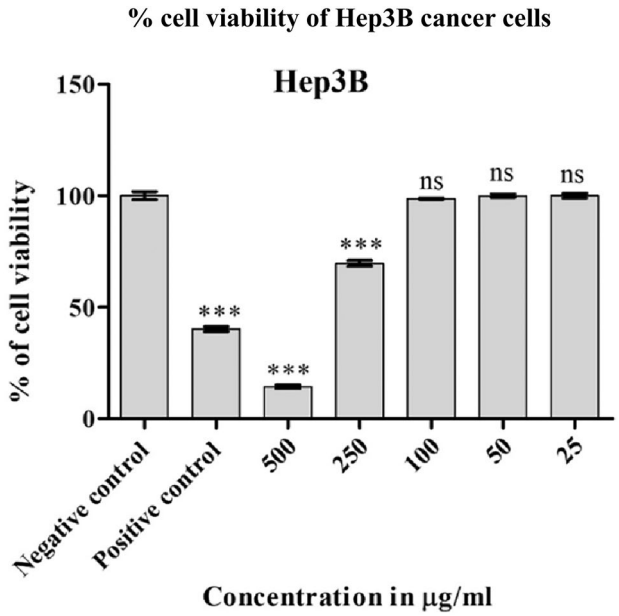

Figure 12. In vitro, cytotoxic activity of liver Hep3B cancer cells treated with various R. intricata aqueous extract concentrations mediated Fe_3O_4 NPs (Negative control = untreated cells; positive control = Doxorubicin 3.87 µg/mL). Results were stated as mean relative expression ± standard error of three replicates. Results were considered significant for ***$P \leq 0.001$ and ns—non-significant.

Hep3B cancer cells and 460.5 µg/mL for PANC1 cancer cells. As the concentration of *R. intricata*-mediated Fe_3O_4 NPs upsurges, cell viability declines. Further, cytotoxicity is predominant against Hep3B liver cancer cells while related to PANC1 pancreatic cancer cells[36] (Table 4).

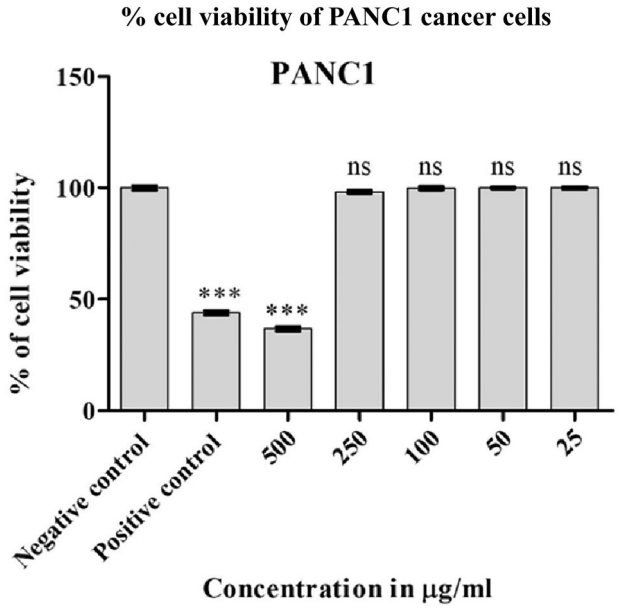

Figure 13. In vitro cytotoxic activity of pancreatic PANC1 cancer cells treated with various R. intricata aqueous extract concentrations mediated Fe_3O_4 NPs (Negative control = untreated cells; positive control = Doxorubicin 8 µg/mL). Results were stated as mean relative expression ± standard error of three replicates. Results were considered significant for $^{***}P \leq 0.001$ and ns—non-significant.

Concentration of *R. intricata*-mediated Fe_3O_4 NPs (µg/mL)	% of cell viability of Hep3B cancer cells			Mean	Standard Deviation	Standard Error
500	**15.67**	**14.36**	**13.05**	**14.36**	**1.31**	**0.75**
250	70.23	71.54	67.36	69.71	2.14	1.24
100	98.96	99.22	97.91	98.69	0.69	0.40
50	100.52	98.43	101.04	100.00	1.38	0.80
25	100.00	101.83	98.17	100.00	1.83	1.06
Negative control	102.87	100.52	96.61	100.00	3.17	1.83
Positive control	40.73	41.78	38.12	40.21	1.88	1.09

Table 3. Statistical analysis of MTT cell proliferation assay results against Hep3B cancer cells.

Concentration of *R. intricata*-mediated Fe_3O_4 NPs (µg/mL)	% of cell viability of PANC1 cancer cells			Mean	Standard deviation	Standard error
500	**36.88**	**35.00**	**38.44**	**36.77**	**1.72**	**0.99**
250	96.88	98.44	99.38	98.23	1.26	0.73
100	98.75	99.38	101.56	99.90	1.48	0.85
50	99.06	100.31	100.63	100.00	0.83	0.48
25	100.00	100.94	99.06	100.00	0.94	0.54
Negative control	98.13	100.31	101.56	100.00	1.74	1.01
Positive control	42.19	44.38	45.31	43.96	1.60	0.9

Table 4. Statistical analysis of MTT cell proliferation assay results against PANC1 cancer cells.

% cell viability of PANC1 *cancer* cells

Cancer cell morphology analysis

Morphological changes of *R. intricata* mediated Fe_3O_4 NPs treated Hep3B and PANC1 cancer cells were visualized under a phase contrast microscope (Figs. 14 and 15). Control cells (untreated) without NPs displayed no alterations in structure with pure and monodispersed and fine matured cells (Figs. 14a and 15a). But the cancer cells treated with *Rosenvingea intricata* mediated Fe_3O_4 NPs (Figs. 14b–f and 15b–f) showed important morphological alterations such as asymmetrical morphology, engorged cells, and cell agglomeration thus confirming

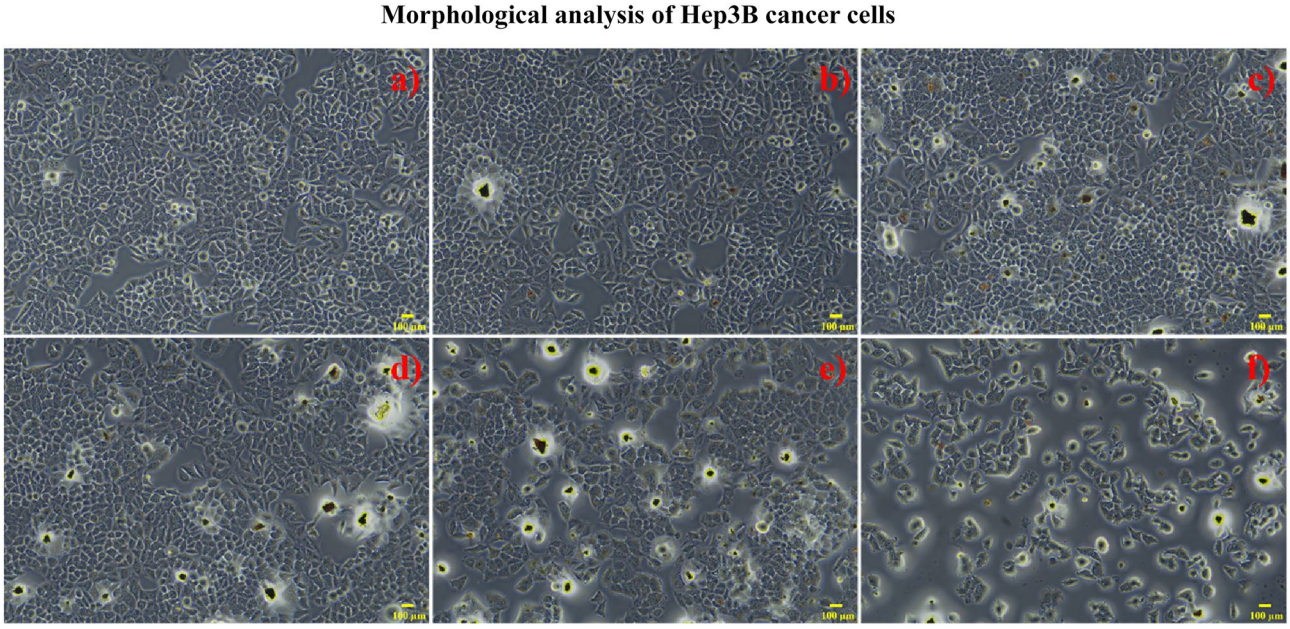

Figure 14. Cell morphological analysis of different concentrations of *R. intricata* aqueous extract mediated Fe_3O_4 NPs {(**a**) 0 µg/mL, (**b**) 25 µg/mL, (**c**) 50 µg/mL, d) 100 µg/mL, (**e**) 250 µg/mL and (**f**) 500 µg/mL} against Hep3B human liver cancer cell line.

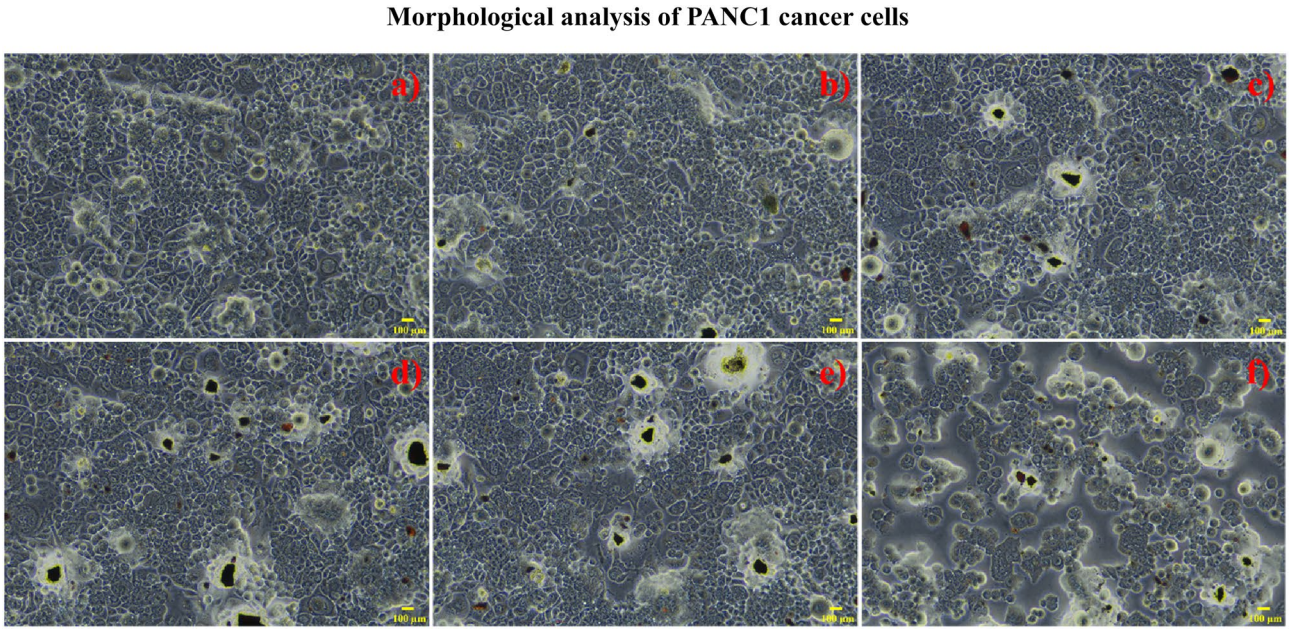

Figure 15. Cell morphological analysis of different concentrations of *R. intricata* aqueous extract mediated Fe_3O_4 NPs {(**a**) 0 µg/mL, (**b**) 25 µg/mL, (**c**) 50 µg/mL, (**d**) 100 µg/mL, (**e**) 250 µg/mL and (**f**) 500 µg/mL} against PANC1 human pancreatic cancer cell line.

the reduction in the number of viable cells, detached cells and changed the morphology of Hep3B and PANC1 cancer cells[37,38].

Morphological analysis of PANC1 *cancer* cells

Apoptotic analysis

Obtained results depicted exceptional apoptotic effect after 24 h treatment with *R. intricata* mediated Fe_3O_4 NPs. The yellow color cells designated the early apoptotic cells in treated Hep3B and PANC1 cancer cells and colorless cells visualized in control along with green color cells representing healthy cancer cells (Figs. 16 and 17). Apoptotic efficacy of *R. intricata* mediated Fe_3O_4 NPs in Hep3B liver cancer cells and PANC1 pancreatic cancer cells suggestively improved the cell mortality over apoptosis, not necrosis[52]. Normally, apoptosis is characterized by

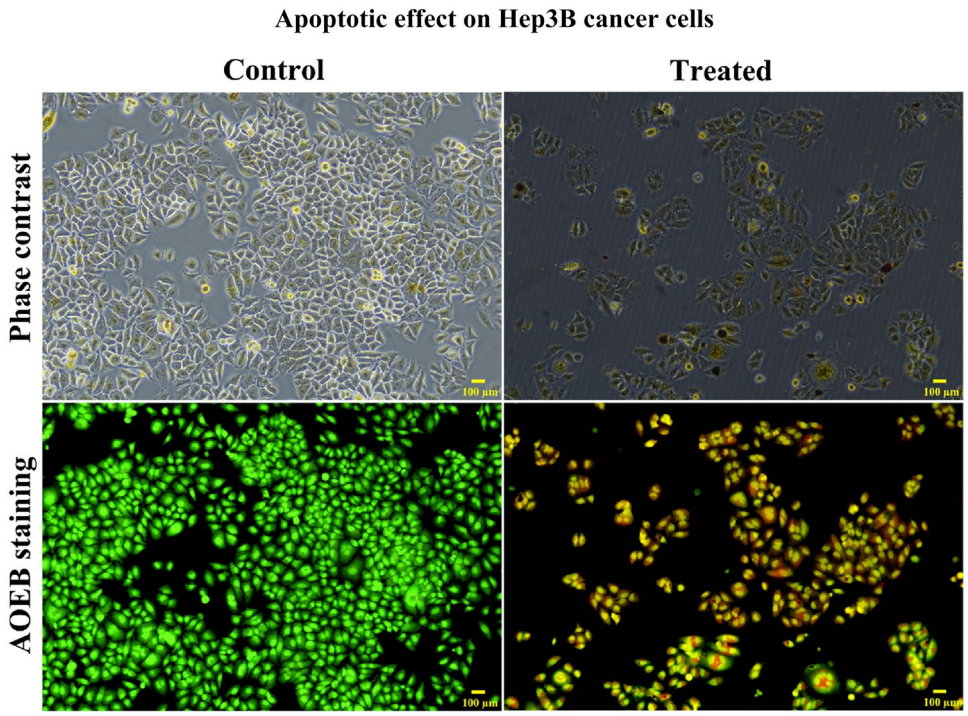

Figure 16. Morphological changes analyzed by phase contrast microscope and apoptotic effect of *R. intricata* aqueous extract mediated Fe_3O_4 NPs (311.7 µg/mL) against Hep3B human liver cancer cell line.

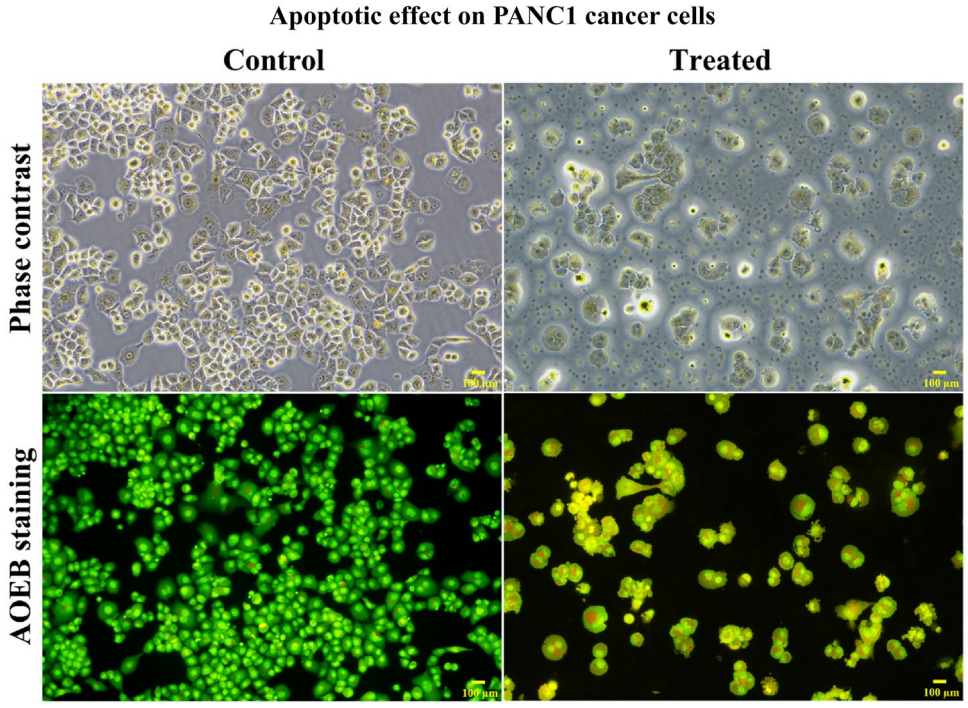

Figure 17. Morphological changes analyzed by phase contrast microscope and apoptotic effect of *R. intricata* aqueous extract mediated Fe_3O_4 NPs (460.5 µg/mL) against PANC1 human pancreatic cancer cell line.

fluorescence intensity after the variations in structural features such as reduced or split chromatin with orange (early apoptosis) and red color (late apoptosis) fluorescence[53]. The above results support the benefit of *R. intricata*-mediated Fe_3O_4 NPs in nanobiology for improved cancer cure.

Apoptotic effect on PANC1 *cancer* cells

From Figs. 16 and 17. it was clear that *R. intricata* mediated Fe_3O_4 NPs showed dose-dependent cytotoxicity against Hep3B and PANC1 cancer cells. Different properties like superparamagnetism ($M_s = 0.90007$ emu/g), smaller size (125 nm), spherical morphology, and surface adherence of biomolecules from *R. intricata* have enabled the cytotoxicity through targeted activity, and easy release of metal ions. Superparamagnetism aids targeted anticancer efficacy due to the magnetic field. This advantage makes them adaptable in targeted drug delivery with fewer side effects. VSM studies found that the R. intricata-mediated Fe_3O_4 NPs are superparamagnetic, augmenting the prospective utilization for targeted drug delivery without affecting the healthy cells[26]. Amidst different shapes of nanomaterials, spherical morphology has notable advantages like uniform surface functionalization, thus excess drugs can be efficiently loaded on the exterior portion of nanomaterials for better biological applications. It is also assumed that the total cell uptake in the drug release system is due to the smaller size of the nanomaterials. Smaller the size of nanomaterials better circulation in the human body with superior penetration via tiny capillaries. Functional groups adhered to the nanomaterials often enhance the biological properties with minimal toxicity to the human body. In the present research, the use of aqueous extract of *R. intricata* has endorsed dose-dependent cytotoxic effects owing to the biomolecules present in it[36,37].

Mechanism of anticancer activity

Based on the review of literature, the hypothesis on the mechanism of anticancer activity by Fe_3O_4 NPs (Fig. 18), suggests that iron ions released generated reactive oxygen species (ROS) into the cancer cell which destructs the mitochondria through oxidative stress. Thereby, inhibiting the replication of DNA resulting in cell death. Nanomaterials with magnetic properties pierce into the nuclear membrane and cause damage to DNA. ROS at excess levels leads to hydrogen bond breakage in the structure of DNA[36,37].

Mechanism of anticancer activity by *R. intricata*-mediated Fe_3O_4 NPs

Comparative studies. The anticancer efficacy of different NPs against various cancer cells is compared with previous reports as given in Table 5.

Conclusion

This is the first report on the usage of marine brown seaweed *R. intricata* for the synthesis of Fe_3O_4 NPs. The use of ferric chloride hexahydrate and aqueous extract of *R. intricata* at moderate conditions produced Fe_3O_4 NPs. Herein, the direct optical band gap was estimated to be 2.30 eV from UV–Vis DRS analysis. From fluorescence studies, band edge emission is observed with a sharp peak at 660 nm. The biomolecules present in the aqueous extract of *R. intricata* played multiple roles as reducing and capping agents for the synthesis of Fe_3O_4 NPs which was proven from FTIR. Crystalline phases were confirmed from XRD with inverse cubic spinel structure. Hydrodynamic size distribution from DLS proved the smaller size of Fe_3O_4 NPs. Irregular morphology with slight aggregates was visualized from HRSEM. Iron and oxygen were present to be maximum from EDX analysis. Sphere-shaped with an average particle size of 125 nm and highly crystalline was witnessed from HRTEM and SAED techniques. The superparamagnetic nature with lesser saturation magnetization (0.90007 emu/g) was confirmed from VSM analysis. From these findings, it is concluded that Fe_3O_4 NPs with magneto-fluorescence properties overlay platform for fluorescent biosensor and magnetic hyperthermia applications in the future.

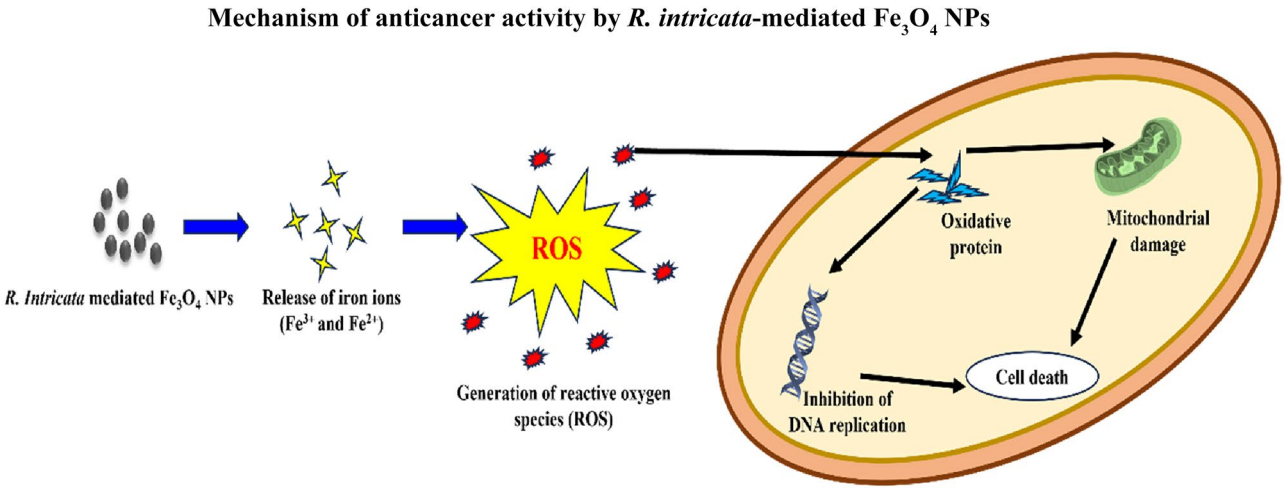

Figure 18. Schematic depiction of the credible mechanism of anticancer activity of *R. intricata*-mediated Fe_3O_4 NPs.

NPs	Seaweed species	Properties of NPs	Cell line used	Observation	References
Pd	*Padina boryana*	Lattice d-space of 0.226 nm	MCF-7 breast cancer cells	Dose-dependent anticancer activity	Sonbol et al.[5]
Ru	*Dictyota dichotoma*	Size 30 nm	HeLa Human cervical cancer cells, MCF-7 human breast cancer cells, and VERO cells	Higher cytotoxicity against HeLa cells	Ali et al.[60]
Au	*Hypnea valentiae*	Round shape with size 7–45 nm	A549 lung cancer cells	EMT signaling pathway genes for control of lung cancer cell growth	Viswanathan et al.[54]
Au	*Ulva rigida* *Cystoseira myrica* *Gracilaria foliifera*	Sphere shaped with size 9–13 nm	MCF-7 breast cancer cells	Highest cytotoxic effect of 86.83%	Algotiml et al.[61]
Au	*Sargassum longifolium*	Sphere shaped with size 10–60 nm	MG-63 human bone cancer cells	Apoptosis due to oxidative stress	Rajeshkumar et al.[62]
Ag	*Ulva rigida* *Cystoseira myrica* *Gracilaria foliifera*	Size 12–24 nm	MCF-7 breast cancer cells	*U. rigida*-mediated Ag NPs showed the highest anticancer value (92.62%)	Algotiml et al.[55]
Ag	*Ulva lactuca*	Spherical size 56 nm	Hep 2 human laryngeal cancer cells, MCF-7 human breast cancer cells, HT 29 human colon cancer cells, and VERO cells	Least toxic against VERO cells	Devi and Bhimba [63]
Se	*Polycladia myrica*	17.48–23.01 nm size	HCT-116 human colon cancer cells	80.57% cytotoxic effect	Abo-Neima et al.[64]
Se	*Polycladia myrica*	Spherical and semi-spherical	PC-3 prostate cancer cells	Maximum inhibitory percent of 80.53%	Touliabah et al.[56]
MgO	*Cystoseira crinita*	Spherical with size 3–18 nm	Caco-2 colon cancer cells	IC_{50} = 113.4 µg/mL	Fouda et al.[57]
CuO	*Undaria pinnatifida*	Circular with size 30 nm	HeLa cervical cancer cells	Dose and time-dependent inhibition with IC_{50} value of 479 µg/mL	Phull et al.[58]
CuO	*Padina boergesenii*	Tetragonal crystalline structure with size 76 nm	A375 skin cancer cells	70% cytotoxic at 100 µg/mL	Balaji et al.[65]
ZnO	*Ulva lactuca* *Stoechospermum marginatum*	Spherical and round-shaped particles	Breast cancer cells	Maximum cell mortality rate (97.34%) for *U. lactuca*-mediated ZnO NPs	Anjali et al.[59]
Fe_3O_4	*Hypnea valentiae*	–	MDA-MB-231 human breast cancer cells and A549 human lung cancer cells	AKT/PI3K pathway regulated cell signaling	Baskar et al.[66]
Fe_3O_4	*Turbinaria conoides*	27.59 nm size	HeLa human cervical cancer cells and DLD1 human colon cancer cells	Potent activity against both HeLa and DLD1 cancer cells	Bensy and Christobel[67]
Fe_3O_4	*Sargassum muticum*	–	Jurkat, MCF-7, HeLa and HepG2 cancer cells of the blood, breast, cervix, and liver cancer cells	Time-response activity	Namvar et al.[25]
Fe_3O_4	*Rosenvingea intricata*	Magnetization value, Ms = 0.90007 emu/g	PANC1 pancreatic and Hep3B liver cancer cells	Dose-dependent activity	This work

Table 5. Comparative analysis of anticancer efficacy of different NPs.

Owed to the inimitable physicochemical properties of Fe_3O_4 NPs, this green synthesized nanomaterial has latent applications in the arena of environmental remediation and biomedicine for catalysis, pollutant detection, cell imaging, and hyperthermia treatment. A further advantage is that the superparamagnetic behavior of Fe_3O_4 NPs aids in the easy retrieval of catalyst from reaction solution with an exterior magnet. Likewise, in the field of biomedicine, this property enables targeted drug delivery. *R. intricata*-mediated Fe_3O_4 NPs augmented the anticancer efficiency against Hep3B and PANC1 cancer cells with IC_{50} values 311.7 and 460.5 µg/mL, correspondingly. Cell morphological analysis and dual staining assay revealed the characteristic apoptotic changes denoting cell death. These findings endorse that the synthesized Fe_3O_4 NPs can be an appropriate alternative for the treatment of human liver and pancreatic cancer. Also, the findings can be converted into technology with suitable testing and more trials in other human cell lines and testing in animal models.

Data availability

The data that support the results of this research are available on request from the corresponding author, Swathi Pon Sakthi Sri V. The data are not publicly available owing to their comprising material that could compromise the privacy of researchers.

Received: 13 May 2024; Accepted: 16 July 2024
Published online: 31 August 2024

References

1. SakthiSri, V. & George, M. Spherical CeO_2 nanoparticles encapsulated with *Nelumbo nucifera* Gaertn. Flower extract and its *in vitro* anticancer activity against HCT 116 human colon cancer cell line. *Indian J. Chem. Technol.* **27**, 153–160 (2020).
2. Ferlay, J. *et al.* Estimating the global cancer incidence and mortality in 2018: GLOBOCAN sources and methods. *Int. J. Cancer.* **144**, 1941–1953 (2019).
3. Dickens, E. & Ahmed, S. Principles of cancer treatment by chemotherapy. *Surgery.* **36**, 134–138 (2018).
4. Fernando, J. & Jones, R. The principles of cancer treatment by chemotherapy. *Surgery.* **33**, 131–135 (2015).

5. Sonbol, H., Ameen, F., AlYahya, S., Almansob, A. & Alwakeel, S. *Padina boryana* mediated green synthesis of crystalline palladium nanoparticles as potential nanodrug against multidrug-resistant bacteria and cancer cells. *Nat. Sci. Rep.* **11**, 5444 (2021).
6. Nikalje, A. P. Nanotechnology and its applications in medicine. *Med. Chem.* **5**, 081–089 (2015).
7. Ameen, F. *et al.* Fabrication of silver nanoparticles employing the cyanobacterium *Spirulina platensis* and its bactericidal effect against opportunistic nosocomial pathogens of the respiratory tract. *J. Mol. Struct.* **3**, 128392 (2020).
8. Khan, I., Saeed, K. & Khan, I. Nanoparticles: properties, applications and toxicities. *Arab. J. Chem.* **12**, 908–931 (2019).
9. Abaid, R. *et al.* Biosynthesizing *Cassia fistula* extract mediated silver nanoparticles for MCF-7 cell lines anti-cancer assay. *ACS Omega.* **8**, 17317–17326 (2023).
10. Endeshaw, S. B. *et al. Croton macrostachyus* leaf extract mediated green synthesis of ZnO nanoparticles and ZnO/CuO nanocomposites for the enhanced photodegradation of methylene blue dye with the COMSOL simulation model. *ACS Omega.* **9**, 559–572 (2024).
11. Win, T. T., Khan, S., Bo, B., Zada, S. & Fu, P. C. Green synthesis and characterization of Fe_3O_4 nanoparticles using *Chlorella*-K01 extract for potential enhancement of plant growth stimulating and antifungal activity. *Nat. Sci. Rep.* **11**, 21996 (2021).
12. Soureshjani, P. T., Shadi, A. & Mohammadsaleh, F. Algae-mediated route to biogenic cuprous oxide nanoparticles and spindle-like $CaCO_3$: A comparative study, facile synthesis, and biological properties. *RSC Adv.* **11**, 10599–10609 (2021).
13. Telebian, S., Shahnavaz, B., Nejabat, M., Abolhassani, Y. & Rassouli, F. B. Bacterial-mediated synthesis and characterization of copper oxide nanoparticles with antibacterial, antioxidant, and anticancer potentials. *Front. Bioeng. Biotechnol.* **11**, 1140010 (2023).
14. Ghosh, S., Ahmad, R., Banerjee, K., AlAjmi, M. F. & Rahman, S. Mechanistic aspects of microbe-mediated nanoparticle synthesis. *Front. Microbiol.* **12**, 638068 (2021).
15. Molnár, Z. *et al.* Green synthesis of gold nanoparticles by thermophilic filamentous fungi. *Nat. Sci. Rep.* **8**, 3943 (2018).
16. Wang, D. *et al.* Fungus-mediated green synthesis of nano-silver using *Aspergillus sydowii* and its antifungal/antiproliferative activities. *Nat. Sci. Rep.* **11**, 10356 (2021).
17. Sharma, A., Sagar, A., Rana, J. & Rani, R. Green synthesis of silver nanoparticles and its antibacterial activity using fungus *Talaromyces purpureogenus* isolated from *Taxus baccata* Linn. *Micro and Nano Syst. Lett.* **10**, 2 (2022).
18. Nuzzo, A., Hosseinkhani, B., Boon, N., Zanaroli, G. & Fava, F. Impact of bio-palladium nanoparticles (bio-Pd NPs) on the activity and structure of a marine microbial community. *Environ. Pollut.* **220**, 1068–1078 (2017).
19. Al-Saif, S. S. A., Abdel-Raouf, N., El-Wazanani, H. A. & Aref, I. A. Antibacterial substances from marine algae isolated from Jeddah coast of Red Sea Saudi Arabia. *Saudi J. Biol. Sci.* **21**, 57–64 (2014).
20. Ibraheem, I. B. M., Alharbi, R. M., Abdel-Raouf, N. & Al-Enazi, N. M. Contributions to the study of the marine algae inhabiting Umluj Seashore, Red Sea. *Beni-Suef Univ. J. Basic Appl. Sci.* **3**, 278–285 (2014).
21. Karthick, P., Ramesh, C. & Mohanraju, R. A checklist of seaweeds of the Andaman and Nicobar Islands, India: A way forward for seaweed cultivation, food, and drug applications. *Environ. Monit. Assess.* **193**, 1–17 (2021).
22. Abdelwahab, R. Therapeutic and pharmaceutical application of seaweeds. *Biotechnol. Appl. Seaweeds. Chapter* **5**, 85–116 (2017).
23. Periera, L. Seaweeds as source of bioactive substances and skin care therapy, cosmeceuticals, algotheraphy, and Thalassotherapy. *Cosmetics.* **5**, 68 (2018).
24. Martins, R. M. *et al.* Macroalgae extracts from Antarctica have antimicrobial and anticancer potential. *Front. Microbiol.* **9**, 1–10 (2018).
25. Namvar, F. *et al.* Cytotoxic effect of magnetic iron oxide nanoparticles synthesized via seaweed aqueous extract. *Int. J. Nanomed.* **9**, 2479–2488 (2014).
26. SakthiSriV, S. P. & George, M. In vitro anticancer and antitubercular activities of cellulose-magnetite nanocomposite synthesized using deep eutectic solvent as a dispersant. *J. Mater. Nanosci.* **8**, 1–10 (2021).
27. Ali, A. *et al.* Synthesis, characterization, applications, and challenges of iron oxide nanoparticles. *Nanotechnol. Sci. Appl.* **19**, 49–67 (2016).
28. Yang, Y. *et al.* Identification and characterization of marine seaweeds for biocompounds production. *Environ. Technol. Innov.* **24**, 101848 (2021).
29. Jha, B., Reddy, C. R. K., Thakur, M. C. & Rao, M. U. *Seaweeds of India: the diversity and distribution of seaweeds of the Gujarat coast* 198 (Springer, Dordrecht, 2009).
30. Rao, P. S. N. & Gupta, R. K. Algae of India, Vol 3: A checklist of Indian Marine Algae (Excluding Diatoms & Dinoflagellates). Botanical Survey of India, Kolkata. pp 93 (2015).
31. Børgesen, F. The marine algae of the Danish West Indies. Part 2. Phaeophyceae. Dansk Botanisk Arkiv **2**(2): 1–68, 44 figs (1914).
32. Krishnamurthy, V. & Baluswami, M. Phaeophyceae of India and neighbourhood Volume I Ectocarpales, Sphacelariales, Dictyotales, Chordariales and Scytosiphonales. pp. [2], i-iv, 1–193, 308 figs, pls I-VI. Chennai: Krishnamurthy Institute of Algology. (2010).
33. Kumar, A. S. & Palanisamy, M. Notes on the additions of phaeophyceae from the coastline of Andhra Pradesh. *Nelumbo* **63**(1), 224–234 (2021).
34. Sobuj, M. K. A. *et al.* Effect of solvents on bioactive compounds and antioxidant activity of *Padina tetrastromatica* and *Gracilaria tenuistipitata* seaweed collected from Bangladesh. *Nat. Sci. Rep.* **11**, 19082 (2021).
35. Guiry, M. D. & Guiry, G. M. 2024. AlgaeBase. World-wide electronic publication, National University of Ireland, Galway. https://www.algaebase.org.
36. SakthiSriV, S. P., Taj, J. & George, M. Facile synthesis of magnetite nanocubes using deep eutectic solvent: An insight to anticancer and photo-Fenton efficacy. *Surf. Interf.* **20**, 100609 (2020).
37. SakthiSriV, S. P. *et al.* Unveiling the photosensitive and magnetic properties of amorphous iron nanoparticles with its application towards decontamination of water and cancer treatment. *J. Mater. Res. Technol.* **15**, 99–118 (2021).
38. Ramalingam, V., Harshavardhan, M., Kumar, S. D. & Devi, S. M. Wet chemical mediated hematite α-Fe_2O_3 nanoparticles synthesis: Preparation, characterization and anticancer activity against human metastatic ovarian cancer. *J. Alloys & Comp.* **834**, 155118–155128 (2020).
39. Chen, Q., Kang, J. & Fu, C. The independence of and associations among apoptosis, autophagy, and necrosis. *Signal Transduct. Targeted Ther.* **3**, 18 (2018).
40. Nidheesh, P. V., Gandhimathi, R., Velmathi, S. & Sanjini, N. S. Magnetite as a heterogenous electro Fenton catalyst for the removal of Rhodamine B from aqueous solution. *RSC Adv.* **4**, 5698–5708 (2014).
41. Rufus, A., Sreeju, N. & Philip, D. Synthesis of biogenic hematite (α-Fe_2O_3) nanoparticles for antibacterial and nanofluid applications. *RSC Adv.* **6**, 94206–94217 (2016).
42. Sadat, M. E. *et al.* Photoluminescence and photothermal effect of Fe_3O_4 nanoparticles for medical imaging and therapy. *Appl. Phys. Lett.* **105**, 91903 (2014).
43. Ali, K. *et al.* Microwave accelerated green synthesis of stable silver nanoparticles with *Eucalyptus globulus* leaf extract and their antibacterial and antibiofilm activity on clinical isolates. *PLoS ONE* **10**, 15 (2015).
44. Li, J. *et al.* A review of the interaction between anthocyanins and proteins. *Food Sci. & Technol. Intern.* **27**, 470–482 (2020).
45. Sánchez-García, F. *et al.* Evolution of volatile compounds and sensory characteristics of edible green seaweed (*Ulva rigida*) during storage at different temperatures. *J. Sci. Food. & Agri.* **99**, 5475–5482 (2019).
46. Wang, T., Jin, X., Chen, Z., Megharaj, M. & Naidu, R. Green synthesis of Fe nanoparticles using eucalyptus leaf extracts for treatment of eutrophic wastewater. *Sci. Total Environ.* **466–467**, 210–213 (2014).

47. Kumar, Y. *et al.* Evaluation of chemical, functional, spectral, and thermal characteristics of *Sargassum wightii* and *Ulva rigida* from Indian coast. *J. Food Qual.* **2021**, 9133464 (2021).
48. Vandanjon, L. *et al.* The use of FTIR spectroscopy as a tool for the seasonal variation analysis and for the quality control of polysaccharides from seaweeds. *Mar. Drugs* **21**, 482 (2023).
49. Wang, Z. *et al.* Water soluble amorphous iron oxide nanoparticles synthesized by a quickly pestling and nontoxic method at room temperature as MRI contrast agents. *Chem. Engin. J.* **235**, 231–235 (2014).
50. SakthiSriV, S. P., Vijayakumar, A. & George, M. Synthesis, optical, morphological and magnetic properties of hematite nanorods in deep eutectic solvent with its antibacterial and photocatalytic applications. *Asian J. Chem.* **31**, 879–885 (2019).
51. SakthiSriV, S. P. & George, M. Spherical CeO2 nanoparticles encapsulated with Nelumbo nucifera Gaertn. Flower extract and its in vitro anticancer activity against HCT 116 human colon cancer cell line. *Indian J. Chem. Technol.* **27**, 153–160 (2020).
52. Sulaiman, G. M., Tawfeeq, A. T. & Naji, A. S. Biosynthesis, characterization of magnetic iron oxide nanoparticles and evaluations of the cytotoxicity and DNA damage of human breast carcinoma cell lines. *Artif. Cells Nanomed. Biotechnol.* **46**, 1215–1229 (2018).
53. Sankar, R. *et al.* Nanostructured delivery system for Suberoylanilide hydroxamic acid against lung cancer cells. *Mater. Sci. Eng. C. Mater. Biol. Appl.* **51**, 362–368 (2015).
54. Viswanathan, S. *et al.* Anti-cancer activity of *Hypnea valentiae* seaweed loaded gold nanoparticles through EMT signaling pathway in A549 cells. *J. Biochem. Systemat. & Ecol.* **107**, 104606 (2023).
55. Algotiml, R. *et al.* Anticancer and antimicrobial activity of biosynthesized Red Sea marine algal silver nanoparticles. *Sci. Rep.* **12**, 2421 (2022).
56. Touliabah, H. E., El-Sheekh, M. M., Elsayed, M. & Makhlof, M. Evaluation of *Polycladia myrica* mediated selenium nanoparticles (PoSeNPS) cytotoxicity against PC-3 cells and antiviral activity against HAV HM175 (Hepatitis A), HSV-2 (Herpes simplex II), and Adenovirus strain 2. *Front. Mar. Sci.* **9**, 1–14 (2022).
57. Fouda, A. *et al.* Enhanced antimicrobial, cytotoxicity, larvicidal, and repellence activities of brown algae, *Cystoseira crinita*-mediated green synthesis of magnesium oxide nanoparticles. *Front. Bioeng. Biotechnol.* **10**, 849921 (2022).
58. Phull, A. R. *et al.* Synthesis, characterization, anticancer activity assessment and apoptosis signaling of fucoidan mediated copper oxide nanoparticles. *Arabian J. Chem.* **14**, 103250 (2021).
59. Anjali, K. P., Sangeetha, B. M., Raghunathan, R., Devi, G. & Dutta, S. Seaweed mediated fabrication of zinc oxide nanoparticles and their antibacterial, antifungal and anticancer applications. *Chem. Slct.* **6**, 647–656 (2021).
60. Ali, M. S., Anuradha, V., Abishek, R., Yogananth, N. & Sheeba, H. *In vitro* anticancer activity of green synthesis ruthenium nanoparticle from *Dictyota dichotoma* marine algae. *NanoWorld J.* **3**, 66–71 (2017).
61. Algotiml, R. *et al.* Anticancer and antimicrobial activity of red sea seaweed extracts-mediated gold nanoparticles. *J. Pure Appl. Microbiol.* **16**, 207–225 (2022).
62. Rajeshkumar, S. *et al.* Apoptotic and antioxidant activity of gold nanoparticles synthesized using marine brown seaweed: An In Vitro study. *Biomed. Res. Int.* **13**, 1–9 (2022).
63. Devi, J. S. & Bhimba, B. V. Anticancer activity of silver nanoparticles synthesized by the seaweed *Ulva lactuca in vitro*. *J. Nanomed. Biotherap. Discovery.* **1**, 1–5 (2012).
64. Abo-Neima, S. E., Ahmed, A. A., El-Sheekh, M. & Makhlof, M. E. M. Polycladia myrica-based delivery of selenium nanoparticles in combination with radiotherapy induces potent in vitro antiviral and in vivo anticancer activities against Ehrlich ascites tumor. *Front. Mol. Biosci.* **10**, 1–15 (2023).
65. Balaji, T. *et al.* Padina boergesenii-mediated copper oxide nanoparticles synthesis, with their antibacterial and anticancer potential. *Biomed.* **11**(2285), 1–15 (2023).
66. Baskar, G. *et al.* Biosynthesis of iron oxide nanoparticles from red seaweed *Hypnea valentiae* and evaluation of their antioxidant and antitumor potential via the AKT/PI3K pathway. *Pro. Biochem.* **141**, 155–169 (2024).
67. Bensy, A. D. V. & Christobel, G. J. Green synthesis of iron nanoparticles using aqueous extract of Turbinaria conoides (J. Agardh) and their anticancer properties. *Current Bot.* **12**, 75–79 (2021).

Acknowledgements

We thank the Ministry of Earth Sciences, Government of India, New Delhi for the support to carry out this research. Our sincere thanks to Dr. G. A. Ramadass, Director, National Institute of Ocean Technology (NIOT), Chennai for the relentless encouragement and rendering the essential laboratory facilities to complete this research. We thank IIT Madras, Chennai, and STIC, Cochin for the instrumental facilities for analysis.

Author contributions

S.P.S.S.V. Conceptualization, Methodology, Data Analysis, and Writing-Original Draft. A.S.K.Y. Resources and Methodology. M.S. Methodology and Software usage. D.K.J. Project administration, Writing-Review and Editing. N.V.V.K. Writing-Review and Editing. G.D. Supervision, Writing-Review, and Editing.

Funding

The authors declare no funding for this research.

Competing interests

The authors declare no competing interests.

Additional information

Correspondence and requests for materials should be addressed to V.S.P.

Reprints and permissions information is available at www.nature.com/reprints.

Publisher's note Springer Nature remains neutral with regard to jurisdictional claims in published maps and institutional affiliations.

Open Access This article is licensed under a Creative Commons Attribution-NonCommercial-NoDerivatives 4.0 International License, which permits any non-commercial use, sharing, distribution and reproduction in any medium or format, as long as you give appropriate credit to the original author(s) and the source, provide a link to the Creative Commons licence, and indicate if you modified the licensed material. You do not have permission under this licence to share adapted material derived from this article or parts of it. The images or other third party material in this article are included in the article's Creative Commons licence, unless indicated otherwise in a credit line to the material. If material is not included in the article's Creative Commons licence and your intended use is not permitted by statutory regulation or exceeds the permitted use, you will need to obtain permission directly from the copyright holder. To view a copy of this licence, visit http://creativecommons.org/licenses/by-nc-nd/4.0/.

© The Author(s) 2024